Nano Research 2015, 8(3): 1026–1037
DOI 10.1007/s12274-014-0584-y
Research Article

ISSN 1998-0124
CN 11-5974/O4

Self-organized metal–semiconductor epitaxial graphene layer on off-axis 4H-SiC(0001)

Debora Pierucci[1], Haikel Sediri[1], Mahdi Hajlaoui[1,2], Emilio Velez-Fort[1,3], Yannick J. Dappe[4], Mathieu G. Silly[2], Rachid Belkhou[2], Abhay Shukla[3], Fausto Sirotti[2], Noelle Gogneau[1], and Abdelkarim Ouerghi[1] (✉)

[1] *CNRS- Laboratoire de Photonique et de Nanostructures, Route de Nozay, 91460 Marcoussis, France*
[2] *Synchrotron-SOLEIL, Saint-Aubin, BP48, F91192 Gif sur Yvette Cedex, France*
[3] *Université Pierre et Marie Curie (CNRS – IMPMC), 4 Pl. Jussieu, 75005 Paris, France*
[4] *Service de Physique de l'Etat Condensé (CNRS URA2464), IRAMIS, CEA Saclay, 91191 Gif-Sur-Yvette, France*

Received: 26 June 2014
Revised: 13 August 2014
Accepted: 15 September 2014

KEYWORDS
epitaxial graphene layer,
monolayer,
bilayer,
band gap opening,
Bernal stacking,
off-axis silicon carbide,
electronic properties

ABSTRACT

The remarkable properties of graphene have shown promise for new perspectives in future electronics, notably for nanometer scale devices. Here we grow graphene epitaxially on an off-axis 4H-SiC(0001) substrate and demonstrate the formation of periodic arrangement of monolayer graphene on planar (0001) terraces and Bernal bilayer graphene on (11$\bar{2}$0) nanofacets of SiC. We investigate these lateral superlattices using Raman spectroscopy, atomic force microscopy/electrostatic force microscopy (AFM/EFM) and X-ray and angle resolved photoemission spectroscopy (XPS/ARPES). The correlation of EFM and ARPES reveals the appearance of permanent electronic band gaps in AB-stacked bilayer graphene on (11$\bar{2}$0) SiC nanofacets of 150 meV. This feature is confirmed by density functional theory (DFT) calculations. The charge transfer between the substrate and graphene bilayer results in an asymmetric charge distribution between the top and the bottom graphene layers opening an energy gap. This surface organization can be thus defined as self-organized metal–semiconductor graphene.

1 Introduction

Graphene exhibits unique properties, making it the material of choice for the observation of novel quantum phenomena and the development of future nanodevices. However, the use of graphene in nanoscale electronics devices requires a modification of its intrinsic semi-metallic nature in order to open an energy gap [1–5]. Among the different techniques used, the synthesis of graphene through thermal decomposition of a SiC substrate is one of the most attractive approaches. In fact, epitaxial graphene shows electronic properties similar to the isolated graphene sheets. In addition epitaxial graphene

Address correspondence to abdelkarim.ouerghi@lpn.cnrs.fr

presents the advantage of a SiC substrate allowing direct device processing, without any transfer steps as in the case of exfoliation [6–10] or metal catalyst chemical vapor deposition (CVD) techniques [11–15].

Many of the desirable properties of graphene are related to its electronic structure with conical π, π* bands (Dirac cone) of vertices touching in a single point at the Fermi level. This makes graphene a gapless semiconductor which is a limiting factor for some applications of graphene in electronics where a sizeable band gap at the Fermi energy is required. Among promising techniques for achieving this goal, the synthesis of nanometer scale ribbons with a band gap induced by quantum confinement [16–18] has been studied in recent years. The common approach to form graphene ribbons is the patterning of preexisting graphene layers [19–21]. However, the different pattern steps induce defects and can degrade electronic properties [22–24]. An alternative consists of directly growing graphene ribbons by thermal decomposition of SiC substrate under specific conditions. This approach has already been demonstrated by performing selective epitaxial growth of few-layer graphene (FLG) on patterned SiC substrates [25, 26] or by controlling the sublimation of Si atoms from non-patterned SiC substrates [27]. Recently Hicks and co-workers [28] have shown that using a patterned SiC(0001) substrate, it is possible to obtain semiconducting graphene ribbons having a band gap energy greater than 0.5 eV. Nevertheless the formation of controlled nanoribbons using this approach requires high-level technological steps. Another possible route relies on laterally altering the graphene band structure by means of an additional periodic potential. In fact, calculations indicate that the lateral superlattice structures may lead to unexpected and potentially useful charge carrier behavior, e.g. gap openings or Fermi velocity anisotropy [3, 28, 29]. To favor this specific lateral graphene band gap structure modulation, the use of off-axis SiC(0001) surfaces appears as a suitable solution. The periodic arrays of atomic steps spaced by flat terraces, as successfully demonstrated on SiC(0001) [30–33], can be considered as a natural "lateral superlattice substrate" for quasi-periodic modulations, with well-defined width hence exhibiting size limited effects.

In this work, we demonstrate the formation of lateral periodic arrangement of bilayer graphene on $(11\bar{2}0)$ nanofacets and monolayer graphene (0001) terraces on off-axis 4H-SiC(0001) using complementary characterization techniques, namely atomic and electrostatic force microscopy (AFM and EFM), Raman spectroscopy, X-ray and angle resolved photoemission spectroscopy (XPS and ARPES). The EFM and ARPES measurement show features due to single and Bernal bilayer graphene. The density functional theory (DFT) study reveals that a SiC facet like $(11\bar{2}0)$ allows the complete decoupling of the bilayer graphene, leading to a gap opening in the bilayer graphene band structure. While the monolayer exhibits a linear dispersion, the AB-stacked bilayer is characterized by two sets of bands due to interlayer interaction and band gap opening and their specific configuration in a lateral metal–semiconductor epitaxial graphene layer is self-organized.

2 Methods

Off-axis 4H-SiC(0001) wafers from NovaSiC with atomically flat surfaces were used to grow high quality epitaxial graphene films by solid state graphitization. The substrate was hydrogen etched (100% H_2) at 1,550 °C to produce well-ordered atomic terraces of SiC. The Si-face SiC(0001) surfaces were deoxidized at 820 °C under semi-vacuum conditions in order to remove the native oxide and any possible surface contamination. Following this surface preparation, the bilayer ribbons graphene were synthesized in atmospheric conditions by radio frequency (RF) heating of the SiC substrate then inducing sublimation of Si atoms and thus carbon enrichment of the surface [34, 35].

The sample was cooled down to room temperature (RT) and transferred *ex situ* to perform different measurements. The surface morphology was studied by AFM, in tapping mode. EFM images of the surface were achieved in lift mode (with a lift scan height of 20 nm) with a Cr/Pt-coated tip characterized with a tip radius of 10 nm.

The graphitization level of the substrate was assessed by micro-Raman spectroscopy performed at RT with a Renishaw spectrometer using a 532 nm

laser focused on the sample by a DMLM Leica microscope with a 50× (NA = 0.75) objective. The Rayleigh diffusion was eliminated by edge filters. XPS/ARPES experiments were carried out on the TEMPO beamline [36] at the SOLEIL French synchrotron facility. The photon source was a HU80 Apple II undulator set to deliver linearly polarized light. The photon energy was selected using a high-resolution plane grating monochromator, with a resolving power $E/\Delta E$ that can reach 15,000 on the whole energy range (45–1,500 eV). The end-station chamber (base pressure = 10^{-10} mbar) is equipped with a modified 200 nm hemispheric electron analyzer (Scienta 200) equipped with a delay line detector [37]. In order to remove contaminants (physisorbed hydrocarbons and water) arising from long exposure to air the sample was first annealed in vacuum ($P = 2 \times 10^{-10}$ mbar) at around 600 °C for 30 min. During the XPS measurements, the photoelectrons were detected at 0° from the sample surface normal $\boldsymbol{n}$ and at 46° from the polarization vector $\boldsymbol{E}$. The C 1s spectra were measured at hν = 340 eV (overall resolution ~100 meV) and hν = 540 eV (overall resolution ~140 meV). For the ARPES measurements, the orientation of the sample and the photon energy of hν = 60 eV were chosen in order to explore the k-space region around the K point along the ΓK direction of the Brillouin zone.

Ab initio calculations were performed using a very efficient DFT localized orbital molecular dynamic technique (FIREBALL) [38–41]. Basis sets of sp^3 for C and Si, and s for H were used with cutoff radii (in atomic units) s = 4.5, p = 4.5 (C), s = 4.8, p = 5.4 (Si) and s = 4.1 (H). In this study we considered supercells of 5 monolayer (ML) SiC(0001) with 2 ML SiC(11$\bar{2}$0). The lateral size roughly corresponds to a 4 × 4 unit cell of graphene. The bottom layer is saturated with hydrogen atoms. On top of the supercell, we set a 4 × 4 AB stacked bilayer of graphene and we performed DFT molecular dynamics at 1,775 K, following the experimental conditions. Once the graphene bilayer left the surface, we relaxed the whole system using a sample of 32 k-points in the Brillouin zone, maintaining the last three bottom layers in bulk positions. The final distance between the graphene planes and the SiC surface was determined using the LCAO-S^2 + vdW formalism [42–44]. A set of 300 special k-points along the Γ–K-M path has been used for the band structure calculations on the relaxed positions.

3 Results and discussions

The important parameters governing the formation of graphene by solid state graphitization from SiC substrates are the annealing temperature at which the sublimation of Si atoms occurs, and the duration of this annealing [45]. On the Si-face SiC substrate it is known that the graphitization takes place preferentially from the step edge and progresses towards the terraces [30, 32]. However, the atomic-step arrangement of the substrate surface is also crucial. In order to optimize the surface morphology of the substrate, the 4H-SiC(0001) substrate was annealed under an argon flux at temperatures higher than those normally used for graphitization so as to favor atomic diffusion and rearrangement [46]. This leads to minimization of the surface energy in well-defined steps and the growth of the specific self-organized lateral graphene layers. By controlling the step-terrace structure and by finely adjusting the temperature and duration of SiC thermal annealing, it is possible to regulate the graphitization level of the surface. Figure 1 shows an AFM image performed in tapping mode and Raman analysis of the surface morphology of off-axis 4H-SiC(0001) after epitaxial graphene growth at 1,500 °C during 10 min and in a 800 mbar Ar atmosphere. The topographic-AFM image (Fig. 1(a)) and the phase-AFM image, (Fig. 1(b)) recorded simultaneously, show a self-ordered stepped surface. The step direction and the terrace width are directly determined by the initial misorientation of the substrate with respect to the crystallographic (0001) plane. The self-ordered surface is described with (0001) terraces spaced by (11$\bar{2}$0) nanofacets [30, 31, 47] at large scale of the sample. The (0001) terraces are characterized by a width of ~700 nm, while the (11$\bar{2}$0) nanofacets are characterized by a width of ~50–70 nm and height of ~30 nm. They are both aligned along the <1$\bar{1}$00> SiC axis. The contrast observed on the AFM phase image, which is directly related to the surface topography and/or material hardness clearly establishes that graphene covers the terraces and that the nanofacets do not have the same thickness. This lateral

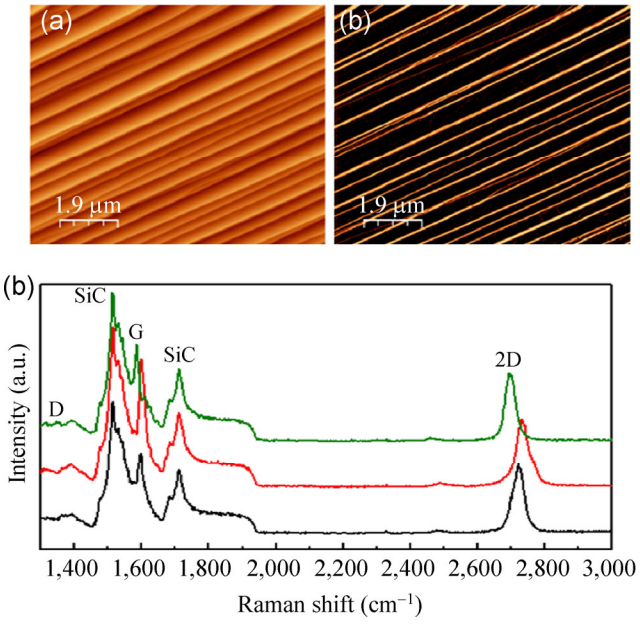

Figure 1 AFM cartography and Raman spectra for epitaxial graphene on off-axis 4H-SiC(0001). (a) AFM image of epitaxial graphene; (b) AFM phase image showing two phase contrasts, at (0001) and (11$\bar{2}$0) SiC facets. Image dimensions are 9 μm × 9 μm; (c) micro-Raman spectra of the D, G and 2D bands collected on the terrace (green and black spectra) and on the step edge (red spectrum), with a 532 nm wavelength excitation and a spatial resolution better than 1 μm.

arrangement of bilayer graphene on (11$\bar{2}$0) nanofacets and monolayer graphene (0001) terraces on a large scale can be considered as a self-organization induced by the stepped SiC substrate. Due to its electronic properties, graphene creates an electron gas, with a significant one-dimensional (1D) or tow-dimensional (2D) lateral modulation. Micro-Raman measurements were carried out under ambient conditions using a Renishaw system with a 532 nm excitation wavelength. A representative Raman spectrum performed on three positions of the sample is presented in Fig. 1(c). The green and black Raman spectra were measured by aligning the incident beam on the widest terraces of the sample while the red spectrum was measured in coincidence with a higher density of step edges. The most prominent Raman features, D, G and 2D bands characterizing a graphene layer are clearly visible. The D peak is a A_{1g} symmetry breathing mode involving phonons near the K point zone boundary, normally not Raman active in defect-less graphene [48, 49]. Its appearance at 1,356 cm^{-1} indicates the presence of defects or structural disorder and step edges. The G peak, corresponding to the in-plane vibration of sp^2 carbon atoms, is a doubly degenerated E_{2g} phonon mode at the Brillouin zone center [49]. The 2D peak, centered at 2,714 cm^{-1}, originates from the double resonant Raman process of the two phonons near the K point zone boundary. The Lorentzian shape of the 2D feature, with a full width at half maximum of around 50 cm^{-1} is the signature of a system with single-band electronic dispersion. It is known that the positions of G and 2D peaks depend on both strain and carrier density (terraces and step edges). The range of values measured for these, shown by two characteristic spectra in Fig. 1(c), indicates the presence of both possibilities and is not surprising given the specific topography of the sample. On the step edges, the blue-shift of the 2D band is correlated with the blue-shift of the G band. It reveals that there is a difference in strain, charge carrier density and/or the number of graphene layers between two surface regions.

For precise local electronic characterization of the graphene surface we use EFM. In particular we seek to determine the relation between the terrace/nanofacet topology as revealed by AFM and the number of graphene layers. EFM (a specific AFM mode) has been demonstrated as a powerful tool for measuring the electric potential distribution with nanometer resolution which allows the variations in the electric field gradient above a sample to be directly measured [50]. EFM images of the surface were achieved in lift mode (with a lift scan height of 20 nm) with a Cr/Pt-coated tip characterized by a tip radius of 10 nm. The macroscale electrical characterization of the epitaxial graphene layers is reported in Fig. 2. The surface morphology (Fig. 2(a)) and the corresponding phase shift (Fig. 2(b)) measured simultaneously for a tip bias voltage of $V = -4$ V under EFM mode are represented. The corresponding profiles performed perpendicular to the steps are presented in Fig. 2(c). A correlation between the localisation of the (0001) terraces and the (11$\bar{2}$0) nanofacets with the variation of the EFM profile is evident. This EFM phase shift Φ, due to the electrostatic interaction between the tip and the sample, evolves with the bias voltage applied. It can

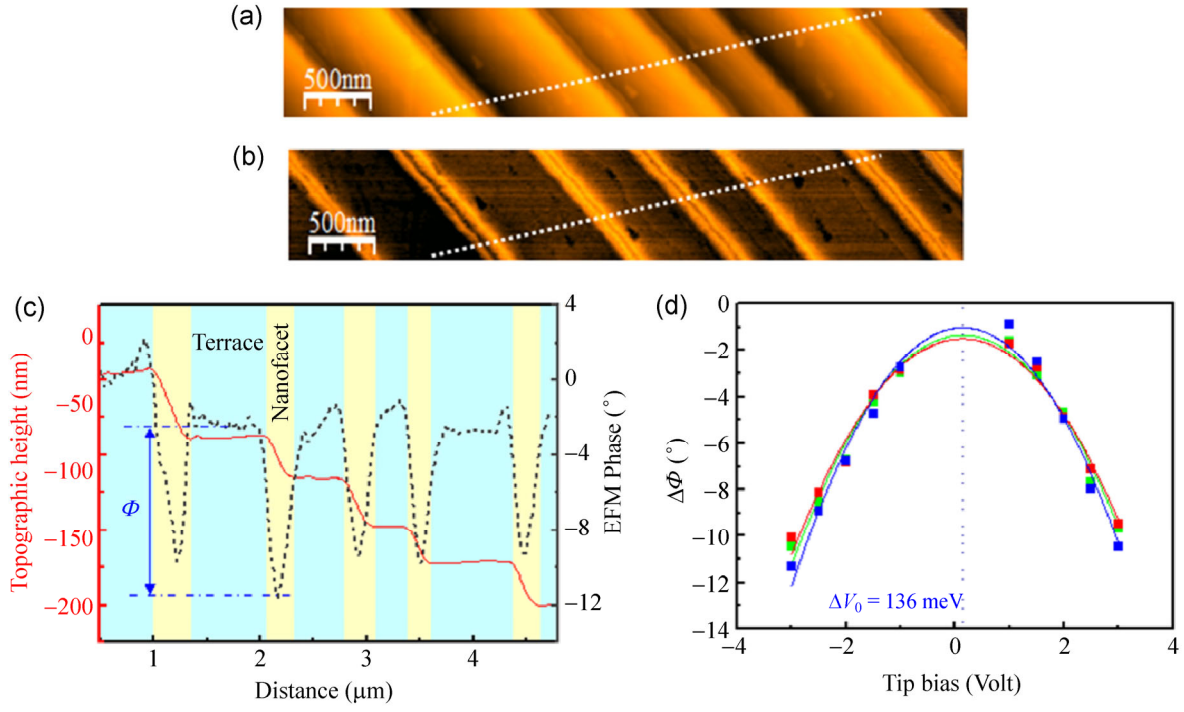

Figure 2 AFM surface morphology (a) and EFM-phase shift (b) images measured simultaneously for a tip bias voltage of $V = -4$ V; (c) profiles performed perpendicular to the steps (dash lines) corresponding to images (a) and (b); (d) variation of the phase shift $\Delta\Phi$ between the (0001) terrace and (11$\bar{2}$0) nanofacets as a function of the tip bias, for three different terrace–nanofacet couples. The variation of work function between the terrace and nanofacet is estimated to be 136 meV for each case.

be expressed as $\Phi = -\frac{Q}{2k}\frac{\mathrm{d}^2C}{\mathrm{d}z^2}\left(V_{\mathrm{tip}} - V_0\right)^2$, where V_{tip} is the bias voltage applied to the tip and V_0 is the local electrostatic potential on the sample's surface, namely the surface potential [50]. The representation of the evolution of the phase shift between the graphene terrace and the graphene nanofacets ($\Delta\Phi_{\mathrm{terrace\text{-}nanofacet}}$), as a function of the tip bias (Fig. 2(d)), can be used to quantify the variation of the electrostatic potential ΔV_0. In fact, the maxima of the parabollic fitting to the data lie to the value of surface potential for each limit. This ΔV_0 variation has been measured for various positions over the surface. For all the terrace–nanofacet couples considered here, from the maxima of the parabolic fit of each data, the value of the surface potential difference between the graphene terrace and nanofacet, $\Delta V_0 = V_{\mathrm{terrace}} - V_{\mathrm{nanofacet}}$, is estimated as ~136 ± 4 mV. The surface potential is related to the work function and is expressed as $e \cdot \Delta V_0^{\mathrm{measured}} = W_{\mathrm{tip}} - W_{\mathrm{sample}}$, where W_{tip} and W_{sample} are the work functions of the tip and the sample surface respectively, and e is the elementary charge [50, 51]. Hence, we estimate that the work function difference between the terrace and nanofacet is ~136 ± 4 meV. This value is in agreement with the increase in the work function of a bilayer graphene with respect to a single layer as previously measured by Kelvin probe force microscopy [52] or EFM techniques [50, 51]. In conclusion, we can describe the surface as constituted by a (0001) terrace covered by monolayer graphene spaced by 2 ML-thick (11$\bar{2}$0) nanofacets.

We also used XPS and ARPES experiments to probe the electronic properties of the sample (Figs. 3 and 4). The XPS measurements performed over a wide energy range show the presence of C 1s, Si 2s, and Si 2p peak intensities on the graphene sample epitaxially grown on a SiC substrate. No other element was detected in our spectra. In particular for the C 1s, the depth position of the corresponding species within the surface was identified by varying the incident photon energy and thus changing the surface sensitivity. The different components contributing to the spectra were decomposed by a curve fitting procedure. The

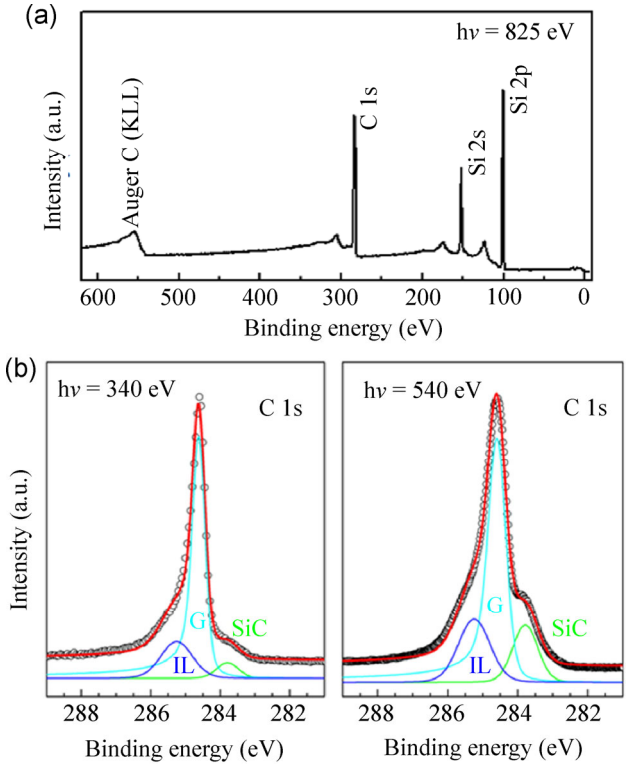

Figure 3 (a) XPS spectra of the graphene layer on off-axis 4H-SiC(0001); (b) C 1s XPS spectra for epitaxial graphene at hν = 340 (left) and 530 eV (right). The take off angle of the electron with respect to the surface normal is 0°. The bottom spectra were fitted using a Doniach–Sunjic line shape analysis.

experimental data points are displayed with dots while the solid line is the envelope of the fitted components. The C 1s core level spectra for two different photon energy (hν = 340 and 540 eV), are compared in Fig. 3(b). In both cases the C 1s spectrum shows three components at 283.4, 284.4, and 284.9 eV in binding energy. The ratio between components at 284.4 and 283.4 eV increases with the photon energy. These components are attributed to the SiC bulk (noted SiC), the graphene layer (noted G), and the interface layer (noted I), respectively [30, 53, 54]. The sharp C 1s peak, labeled G, located at 284.4 eV in binding energy, indicates the presence of sp^2 hybridized C–C bonds. This component has been fitted using a Doniach–Sunjic line shape with an asymmetry factor α of 0.1 and a FWHM of 0.45 eV. Assuming that the graphene–SiC sample can be modeled as a semi-infinite SiC substrate with a uniform graphene overlayer, the thickness can be calculated from the ratio between the intensity of the G and SiC components [55] extracted from XPS data. This ratio fits well with an exponential decay of roughly 1.3 ML of carbon covering. This value is in agreement with a mixed situation between monolayer graphene and bilayer graphene on off-axis 4H-SiC confirming the interpretation of AFM/EFM images in terms of local film thickness and structure. We further make an average evaluation of the surface electronic structure by ARPES. ARPES provides a means to identify the thickness of the majority species in the film, not only through a method that gives lateral resolution, but also by the thickness sensitivity in a "fingerprint" manner. A single linearly dispersing π band at the K point of the Brillouin zone, near the so-called Dirac point E_D, is characteristic of the single layer, while the bilayer spectrum has an extra set of bands due to the interlayer splitting brought about by the close proximity of the layers. ARPES and the second derivative of the ARPES data as a function of energy and electron wave vector, shown in Fig. 4, were recorded at photon energy of 60 eV, near the K point of the Brillouin zone, along the MKΓ direction. Three separate bands are observed in the measured photoemission pattern, one from the monolayer band, and two from the branches of the bilayer bands. While the single layer is characterized by a linear dispersion as indicated by the pink arrow in Figs. 4(a) and 4(b), the double layer exhibits two sets of bands due to interlayer interaction (green arrows). ARPES data show features due to both single and bilayer graphene regions [56]. The band structure is in perfect agreement with the presence of monolayer graphene on the planar (0001) face of SiC and bilayer graphene ribbons on the (11$\bar{2}$0) facets of the steps[31, 47].

Figure 4(c) shows the energy distribution curves (EDCs) along the ΓK direction for the graphene in off-axis SiC. This figure reveals broad line-shapes, which cause an overlap of the intensity tails from the top of the valence band and the bottom of the conduction band. Nevertheless, the dispersion of the bands and the electronic gap between the π and π* states are well resolved. In particular from the fitting of the π and π* peaks positions taken at the K point (Fig. 4(d)) in the EDCs, we obtain an energy gap value Δ for 2 ML graphene nanofacet of about 150 meV. The position of the Dirac point at 0.5 and 0.3 eV below the Fermi energy indicates an *n*-type doping

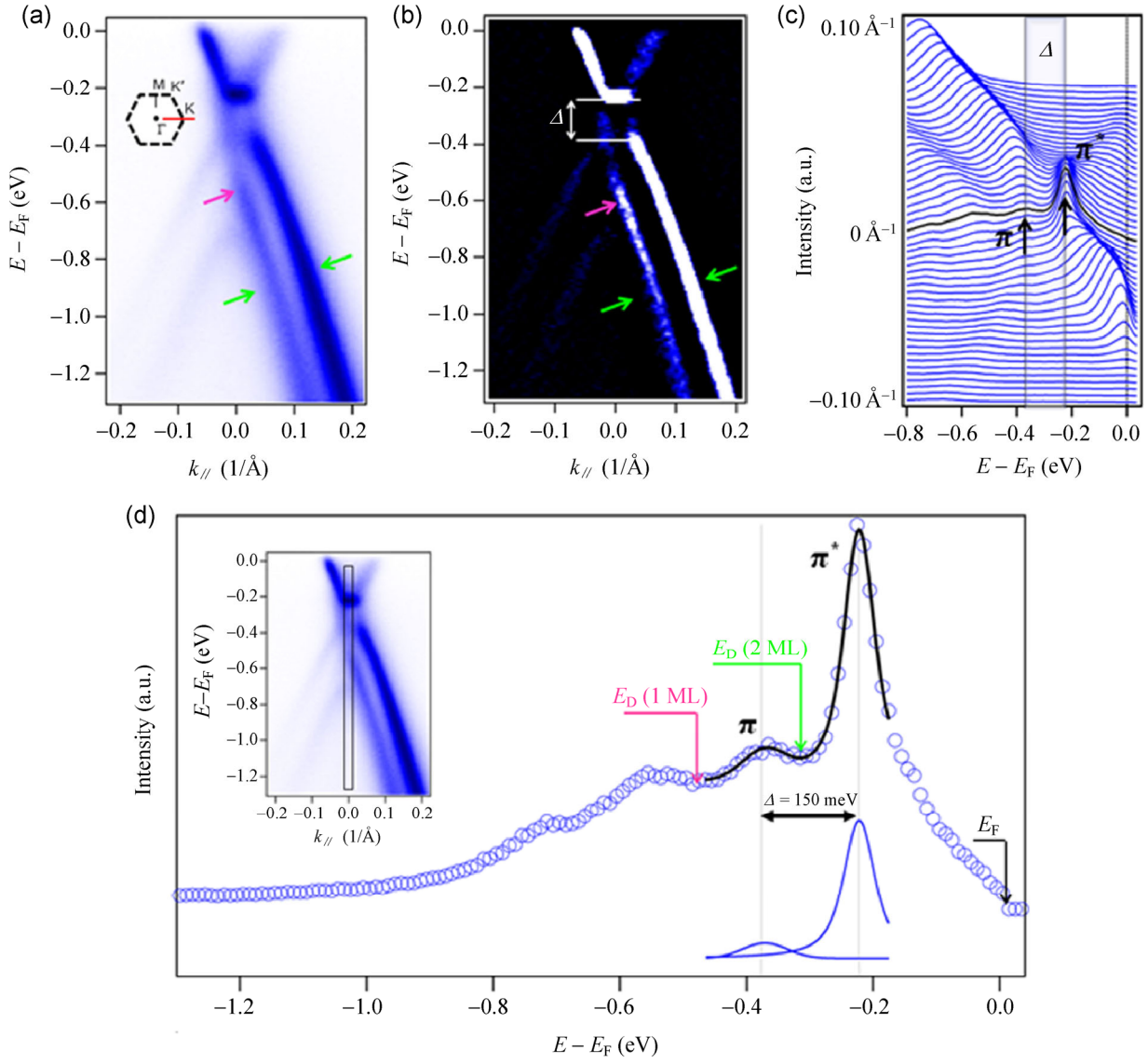

Figure 4 (a) and (b) 2D band structure map and second derivative along the ΓK direction, obtained by ARPES (hν = 60 eV) at room temperature, on epitaxial graphene on off-axis 4H-SiC(0001). The inset of (a) shows the Brillouin zone of graphene and the horizontal line in the ΓK direction presents the measurement geometry in the k-space. (c) and (d) ARPES intensity integrated spectra as a function of the binding energy, extracted from the 2D ARPES map.

($n \approx 10^{13}$ and 5×10^{12} cm^{-2}) for monolayer and bilayer graphene respectively. These inhomogeneities of the band structure are reflected in the macroscopic work function variation measured by EFM.

We have also performed DFT calculations that confirm these results. In Fig. 5(a), we represent the equilibrium configuration of the decoupled AB stacked bilayer graphene on the 2 ML SiC(11$\bar{2}$0)/5 ML SiC(0001). The system was first allowed to evolve freely in molecular dynamics at 1,775 K, and then the geometry was optimized at room temperature to reproduce the conditions of the experimental measurements. We observed that the bilayer graphene is totally decoupled from the surface and the interaction is now ruled by van der Waals interactions. In Fig. 5(b) we represent the corresponding partial band structure for the bilayer graphene along the ΓKM direction. This band structure shows a band gap opening of around 115 meV. This value is slightly smaller than the experimental one, as expected in DFT where the electronic gaps are always underestimated. The doping is unfortunately not so well reproduced since we find an almost

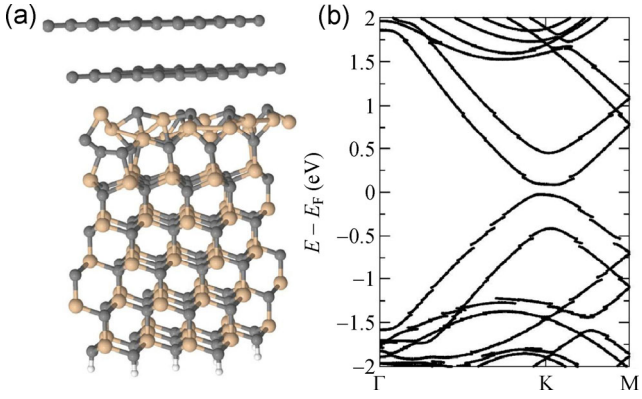

Figure 5 (a) Geometric representation of the equilibrium configuration of the bilayer graphene on SiC(11$\bar{2}$0)/SiC(0001) obtained by DFT calculations; (b) bilayer graphene band structure around the K point showing the gap opening of the graphitic layers.

electronically neutral bilayer graphene band structure. This is due to a well-known problem within the DFT formalism, where the doping is highly dependent on the choice of the exchange-correlation potential. Therefore, a quantitative evaluation of the doping remains a difficult challenge in this frame [57, 58]. Nevertheless, these calculations give the correct tendency of the underlying physical processes, such as the decoupling of the bilayer graphene and the asymmetric charge transfer. Indeed, looking at the electronic charges at each graphene plane, we can estimate the electronic transfer from the substrate to the graphene bilayer. This transfer, through its resulting electric field is responsible for the gap opening in the structure. From our calculations, this electric field can be estimated to be around 0.13 V·Å^{-1}. This value is probably underestimated in the same manner as the doping, but is sufficient to semi-quantitatively explain the gap opening.

Our results show two features: (i) An epitaxial monolayer graphene on a buffer layer on the (0001) terraces and (ii) bilayer graphene on (11$\bar{2}$0) facets of SiC [47]. This structure is of crucial importance because it consists of electronically dissimilar polymorphs, which are lattice matched such that they form chemically homogeneous atomic and electronic heterostructures between mono- and bilayer graphene (Fig. 6). In fact, this offers two distinct advantages: First, the bilayer locally alters the electrical properties of a monolayer grown on off-axis SiC(0001), opening up the possibility of producing electron gases with a significant 1D or 2D lateral potential modulation along the SiC step edges [34]. Secondly, this bilayer induces local modification of the electrical characteristics of epitaxial graphene on SiC steps, since it should trigger intrinsic scattering mechanisms that are related to areas of unequal doping and unequal number of graphene layers [34].

Another attractive aspect is the presence of self-organized semiconductor bilayer graphene, generated

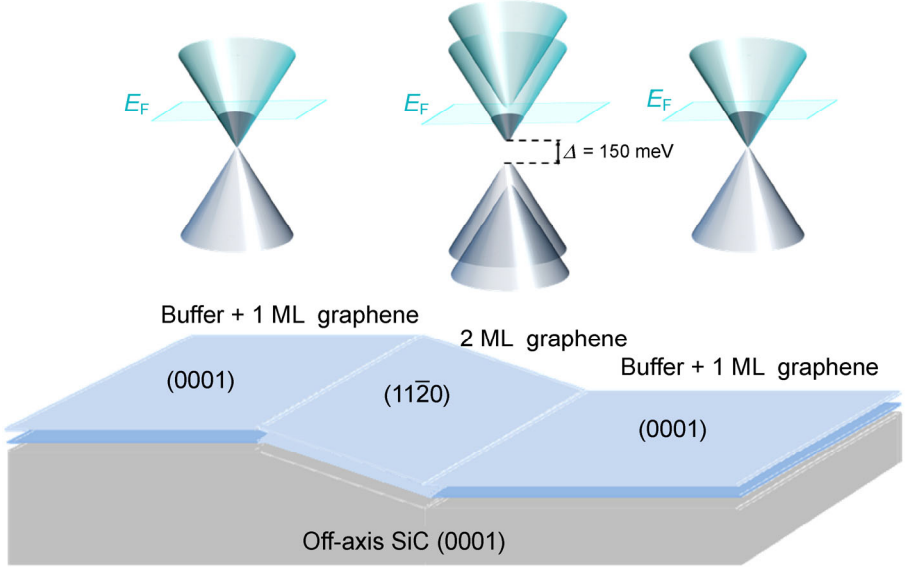

Figure 6 Schematic 2D heterostructure of epitaxial graphene on off-axis 4H-SiC(0001) and the band structure of monolayer graphene on (0001) SiC and bilayer graphene on (11$\bar{2}$0) SiC facets.

at the nanofacets (Fig. 6). The presence of bilayer graphene at nanofacets is of crucial importance since it introduces the possibility of an electronic band gap [29, 59], making it a semiconductor, due to the intrinsic charge asymmetry between the layers from the SiC substrate. In our case, we have a band gap of about 150 meV. Two hypotheses can explain the development of this band gap opening:

(i) Lateral quantum confinement of bilayer graphene on SiC nanofacets. AFM measurements show that the size of these ribbons is about 50 nm. However, numerous studies of graphene nanostructures have demonstrated that a sizeable band gap can be expected only if their sizes are less than 10 nm in at least one dimension [19], to reproduce quantum confinement, which is not the case here.

(ii) Breaking of the inversion symmetry in bilayer graphene. By applying an external electric field normal to the bilayer graphene plane, a band gap can be opened in the Bernal stacking (AB-stacking) bilayer graphene. It has been shown that charge transfer in bilayer graphene on SiC(0001) can induce a band gap opening [29]. Our ARPES study shows a band gap and a charge transfer between the $(11\bar{2}0)$ nanofacet and bilayer graphene. This charge transfer is in agreement with a recent study of monolayer graphene on non polar SiC$(11\bar{2}0)$ [31, 57]. These results are confirmed by our DFT calculations, which provide an estimate of the electric field value. Consequently, inversion symmetry breaking in bilayer graphene by charge transfer doping is at the origin of the band gap opening in our case.

The organization of monolayer and bilayer graphene planar structure on a large scale is of particular interest: (i) The two different electronic structures related to the monolayer and bilayer graphene, such as the charge carriers and strain at the step edges, may act as wide reaction sites to obtain selected patterned molecular adsorption even when graphene binds only weakly to them, and (ii) the two structures with different Landau level sequences (and different Berry's phases for charge carriers) may be used in tuning transport properties, of particular interest being a planar heterostructure with no analog in conventional 2DEG III/V.

4 Conclusions

We have developed a methodology to synthesize a new 2D heterostructure based on a self organized monolayer–bilayer graphene on off-axis 4H-SiC(0001). The epitaxial monolayer and bilayer graphene layers were evidenced by AFM/EFM, Raman measurements and XPS spectroscopy. Our ARPES measurements reveal that the graphene layer consists of micrometer-sized domains of semiconducting and metallic phases that form coherent interfaces with one another. DFT calculations confirm the decoupling of the bilayer graphene from the SiC surface, leading to a gap opening in the upper graphene sheet. This gap opening is mainly attributed to the charge transfer between the SiC substrate and the bilayer graphene structure, with an estimated resulting electric field of around 0.13 $V \cdot Å^{-1}$. Such a modification of the intrinsically semi-metallic nature of graphene to introduce a band gap is essential for the use of graphene in nanoscale electronics applications working at room temperature, such as field-effect transistors. The two polymorphs of monolayer and bilayer graphene which allow formation of coherent electronic heterostructures represent a unique characteristic of this material that may be exploited for novel molecular functionalities.

Acknowledgements

The authors thank the French National Research Agency (ANR) SUPERTRAMP project and LABEX NanoSaclay for funding.

References

[1] Costa Girão, E.; Liang, L. B.; Cruz-Silva, E.; Filho, A. G. S.; Meunier, V. Emergence of a typical properties in assembled graphene nanoribbons. *Phys. Rev. Lett.* **2011**, *107*, 135501.

[2] Sprinkle, M.; Ruan, M.; Hu, Y.; Hankinson, J.; Rubio-Roy, M.; Zhang, B.; Wu, X.; Berger, C.; de Heer, W. A. Scalable templated growth of graphene nanoribbons on SiC. *Nat. Nanotechnol.* **2010**, *5*, 727–731.

[3] Zhou, S. Y.; Gweon, G. H.; Fedorov, A. V.; First, P. N.; de Heer, W. A.; Lee, D. H.; Guinea, F.; Castro Neto, A. H.; Lanzara, A. Substrate-induced bandgap opening in epitaxial graphene. *Nat. Mater.* **2007**, *6*, 770–775.

[4] Son, Y. W.; Cohen, M. L.; Louie, S. G. Energy gaps in graphene nanoribbons. *Phys. Rev. Lett*. **2006**, *97*, 216803.

[5] Chen, Z. H.; Lin, Y. M.; Rooks, M. J.; Avouris, P. Graphene nano-ribbon electronics. *Physica E Lowdimens Syst. Nanostruct*. **2007**, *40*, 228–232.

[6] Novoselov, K. S.; Geim, A. K.; Morozov, S. V.; Jiang, D.; Zhang, Y.; Dubonos, S. V.; Grigorieva, I. V.; Firsov, A. A. Electric field effect in atomically thin carbon films. *Science* **2004**, *306*, 666–669.

[7] Stankovich, S.; Dikin, D. A.; Dommett, G. H. B.; Kohlhaas, K. M.; Zimney, E. J.; Stach, E. A.; Piner, R. D.; Nguyen, S. T.; Ruoff, R. S. Graphene-based composite materials. *Nature* **2006**, *442*, 282–286.

[8] Hass, J.; de Heer, W. A.; Conrad, E. H. The growth and morphology of epitaxial multilayer graphene. *J. Phys.: Condens. Matter* **2008**, *20*, 323202.

[9] Varchon, F.; Feng, R.; Hass, J.; Li, X.; Nguyen, B. N.; Naud, C.; Mallet, P.; Veuillen, J. Y.; Berger, C.; Conrad, E. H. et al. Electronic structure of epitaxial graphene layers on SiC: Effect of the substrate. *Phys. Rev. Lett*. **2007**, *99*, 126805.

[10] Forbeaux, I.; Themlin, J. M.; Debever, J. M. Heteroepitaxial graphite on 6H-SiC (0001): Interface formation through conduction-band electronic structure. *Phys. Rev. B* **1998**, *58*, 396–406.

[11] Somani, P. R.; Somani, S. P.; Umeno, M. Planer nano-graphenes from camphor by CVD. *Chem. Phys. Lett*. **2006**, *430*, 56–59.

[12] Sutter, P. W.; Flege, J. I.; Sutter, E. A. Epitaxial graphene on ruthenium. *Nat. Mater*. **2008**, *7*, 406–411.

[13] Reina, A.; Jia, X. T.; Ho, J.; Nezich, D.; Son, H.; Bulovic, V.; Dresselhaus, M. S.; Kong, J. Large area, few-layer graphene films on arbitrary substrates by chemical vapor deposition. *Nano Lett*. **2009**, *9*, 30–35.

[14] Wang, J. J.; Zhu, M. Y.; Outlaw, R. A.; Zhao, X.; Manos, D. M.; Holloway, B. C. Synthesis of carbon nanosheets by inductively coupled radio-frequency plasma enhanced chemical vapor deposition. *Carbon* **2004**, *42*, 2867–2872.

[15] Wang, J. J.; Zhu, M. Y.; Outlaw, R. A.; Zhao, X.; Manos, D. M.; Holloway, B. C.; Mammana, V. P. Free-standing subnanometer graphite sheets. *Appl. Phys. Lett*. **2004**, *85*, 1265.

[16] Berger, C.; Song, Z. M.; Li, X. B.; Wu, X. S.; Brown, N.; Naud, C.; Mayou, D.; Li, T. B.; Hass, J.; Marchenkov, A. N. et al. Electronic confinement and coherence in patterned epitaxial graphene. *Science* **2006**, *312*, 1191–1196.

[17] Brey, L.; Fertig, H. Electronic states of graphene nanoribbons studied with the Dirac equation. *Phys. Rev. B* **2006**, *73*, 235411.

[18] Nakada, K.; Fujita, M.; Dresselhaus, G.; Dresselhaus, M. S. Edge state in graphene ribbons: Nanometer size effect and edge shape dependence. *Phys. Rev. B* **1996**, *54*17954.

[19] Han, M. Y.; Özyilmaz, B.; Zhang, Y. B.; Kim, P. Energy band-gap engineering of graphene nanoribbons. *Phys. Rev. Lett*. **2007**, *98*, 206805.

[20] Tapasztó, L.; Dobrik, G.; Lambin, P.; Biró, L. P. Tailoring the atomic structure of graphene nanoribbons by STM lithography. *Nat. Nanotechnol*. **2008**, *3*, 397–401.

[21] Han, M. Y.; Brant, J. C.; Kim, P. Electron transport in disordered graphene nanoribbons. *Phys. Rev. Lett*. **2010**, *104*, 056801.

[22] Bolotin, K. I.; Sikes, K. J.; Jiang, Z.; Klima, M.; Fudenberg, G.; Hone, J.; Kim, P.; Stormer, H. L. Ultrahigh electron mobility in suspended graphene. *Solid State Commun*. **2008**, *146*, 351–355.

[23] Hwang, E. H.; Adam, S.; Das Sarma, S. Transport in chemically doped graphene in the presence of adsorbed molecules. *Phys. Rev. B* **2007**, *76*, 195421.

[24] Moser, J.; Barreiro, A.; Bachtold, A. Current-induced cleaning of graphene. *Appl. Phys. Lett*. **2007**, *91* 163513.

[25] Camara, N.; Rius, G.; Huntzinger, J. R.; Tiberj, A.; Mestres, N.; Godignon, P.; Camassel, J. Selective epitaxial growth of graphene on SiC. *Appl. Phys. Lett*. **2008**, *93*, 123503.

[26] Rubio-Roy, M.; Zaman, F.; Hu, Y.; Berger, C.; Moseley, M. W.; Meindl, J. D.; de Heer, W. A. Structured epitaxial graphene growth on SiC by selective graphitization using a patterned AlN cap. *Appl. Phys. Lett*. **2010**, *96*, 082112.

[27] Camara, N.; Huntzinger, J. R.; Rius, G.; Tiberj, A.; Mestres, N.; Pérez-Murano, F.; Godignon, P.; Camassel, J. Anisotropic growth of long isolated graphene ribbons on the C face of graphite-capped 6H-SiC. *Phys. Rev. B* **2009**, *80*, 125410.

[28] Hicks, J.; Tejeda, A.; Taleb-Ibrahimi, A.; Nevius, M. S.; Wang, F.; Shepperd, K.; Palmer, J.; Bertran, F.; Le Fèvre, P.; Kunc, J. et al. A wide-bandgap metal–semiconductor–metal nanostructure made entirely from graphene. *Nat. Phys.* **2013**, *9*, 49–54.

[29] Ohta, T.; Bostwick, A.; Seyller, T.; Horn, K.; Rotenberg, E. Controlling the electronic structure of bilayer graphene. *Science* **2006**, *313*, 951–954.

[30] Ouerghi, A.; Silly, M. G.; Marangolo, M.; Mathieu, C.; Eddrief, M.; Picher, M.; Sirotti, F.; El Moussaoui, S.; Belkhou, R. Large-area and high-quality epitaxial graphene on off-axis SiC wafers. *ACS Nano* **2012**, *6*, 6075–6082.

[31] Nicotra, G.; Ramasse, Q. M.; Deretzis, I.; La Magna, A.; Spinella, C.; Giannazzo, F. Delaminated graphene at silicon carbide facets: Atomic scale imaging and spectroscopy. *ACS Nano* **2013**, *7*, 3045–3052.

[32] Tanaka, S.; Morita, K.; Hibino, H. Anisotropic layer-by-layer growth of graphene on vicinal SiC(0001) surfaces. *Phys. Rev. B* **2010**, *81*, 041406.

[33] Vecchio, C.; Sonde, S.; Bongiorno, C.; Rambach, M.; Yakimova, R.; Raineri, V.; Giannazzo, F. Nanoscale structural characterization of epitaxial graphene grown on off-axis 4H-SiC (0001). *Nanoscale Res. Lett*. **2011**, *6,* 269.

[34] Lalmi, B.; Girard, J. C.; Pallecchi, E.; Silly, M.; David, C.; Latil, S.; Sirotti, F.; Ouerghi, A. Flower-shaped domains and wrinkles in trilayer epitaxial graphene on silicon carbide. *Sci. Rep.* **2014**, *4*, 4066.

[35] Pallecchi, E.; Lafont, F.; Cavaliere, V.; Schopfer, F.; Mailly, D.; Poirier, W.; Ouerghi, A. High electron mobility in epitaxial graphene on 4H-SiC(0001) via post-growth annealing under hydrogen. *Sci. Rep.* **2014**, *4*, 4558.

[36] Polack, F.; Silly, M.; Chauvet, C.; Lagarde, B.; Bergeard, N.; Izquierdo, M.; Chubar, O.; Krizmancic, D.; Ribbens, M.; Duval, J. P. et al. TEMPO: A new insertion device beamline at SOLEIL for time resolved photoelectron spectroscopy experiments on solids and interfaces. *AIP Conf. Proc.* **2010**, *1234*, 185–188.

[37] Bergeard, N.; Silly, M. G.; Krizmancic, D.; Chauvet, C.; Guzzo, M.; Ricaud, J. P.; Izquierdo, M.; Stebel, L.; Pittana, P.; Sergo, R. et al. Time-resolved photoelectron spectroscopy using synchrotron radiation time structure. *J. Synchrotron Radiat*. **2011**, *18*, 245–250.

[38] Lewis, J. P.; Glaesemann, K. R.; Voth, G. A.; Fritsch, J.; Demkov, A. A.; Ortega, J.; Sankey, O. F. Further developments in the local-orbital density-functional-theory tight-binding method. *Phys. Rev. B* **2001**, *64*, 195103.

[39] Lewis, J. P.; Jelínek, P.; Ortega, J.; Demkov, A. A.; Trabada, D. G.; Haycock, B.; Wang, H.; Adams, G.; Tomfohr, J. K.; Abad, E. et al. Advances and applications in the FIREBALL *ab initio* tight-binding molecular-dynamics formalism. *Phys. Status Solidi B* **2011**, *248*, 1989–2007.

[40] Jelínek, P.; Wang, H.; Lewis, J. P.; Sankey, O. F.; Ortega, J. Multicenter approach to the exchange-correlation interactions in *ab initio* tight-binding methods. *Phys. Rev. B* **2005**, *71*, 235101.

[41] Sankey, O. F.; Niklewski, D. J. *Ab initio* multicenter tight-binding for molecular-dynamics simulations and other applications in covalent systems. *Phys. Rev. B* **1989**, *40*, 3979–3995.

[42] Basanta, M. A.; Dappe, Y. J.; Jelínek, P.; Ortega, J. Optimized atomic-like orbitals for first-principles tight-binding molecular dynamics. *Comp. Mater. Sci.* **2007**, *39*, 759–766.

[43] Dappe, Y. J.; Ortega, J.; Flores, F. Intermolecular interaction in density functional theory: Application to carbon nanotubes and fullerenes. *Phys. Rev. B* **2009**, *79*, 165409.

[44] Švec, M.; Merino, P.; Dappe, Y. J.; González, C.; Abad, E.; Jelínek, P.; Martin-Gago, J. A. van der Waals interactions mediating the cohesion of fullerenes on graphene. *Phys. Rev. B* **2012**, *86*, 121407.

[45] Ouerghi, A.; Balan, A.; Castelli, C.; Picher, M.; Belkhou, R.; Eddrief, M.; Silly, M. G.; Marangolo, M.; Shukla, A.; Sirotti, F. Epitaxial graphene on single domain 3C-SiC (100) thin films grown on off-axis. *Appl. Phys. Lett.* **2012**, *101*, 021603.

[46] Michon, A.; Vézian, S.; Ouerghi, A.; Zielinski, M.; Chassagne, T.; Portail, M. Direct growth of few-layer graphene on 6H-SiC and 3C-SiC/Si via propane chemical vapor deposition. *Appl. Phys. Lett.* **2010**, *97*, 171909.

[47] Giannazzo, F.; Deretzis, I.; Nicotra, G.; Fisichella, G.; Spinella, C.; Roccaforte, F.; La Magna, A. Electronic properties of epitaxial graphene residing on SiC facets probed by conductive atomic force microscopy. *Appl. Surf. Sci.* **2014**, *291*, 53–57.

[48] Huang, H.; Wong, S. L.; Tin, C. C.; Luo, Z. Q.; Shen, Z. X.; Chen, W.; Wee, A. T. S. Epitaxial growth and characterization of graphene on free-standing polycrystalline 3C-SiC. *J. Appl. Phys*. **2011**, *110*, 014308.

[49] Pimenta, M. A.; Dresselhaus, G.; Dresselhaus, M. S.; Cançado, L. G.; Jorio, A.; Saito, R. Studying disorder in graphite-based systems by Raman spectroscopy. *Phys. Chem. Chem. Phys*. **2007**, *9*, 1276–1291.

[50] Burnett, T.; Yakimova, R.; Kazakova, O. Mapping of local electrical properties in epitaxial graphene using electrostatic force microscopy. *Nano Lett.* **2011**, *11*, 2324–2328.

[51] Gogneau, N.; Balan, A.; Ridene, M.; Shukla, A.; Ouerghi, A. Control of the degree of surface graphitization on 3C-SiC(100)/Si(100). *Surf. Sci.* **2012**, *606*, 217–220.

[52] Filleter, T.; Emtsev, K. V.; Seyller, T.; Bennewitz, R. Local work function measurements of epitaxial graphene. *Appl. Phys. Lett.* **2008**, *93*, 133117.

[53] Coletti, C.; Emtsev, K. V.; Zakharov, A. A.; Ouisse, T.; Chaussende, D.; Starke, U. Large area quasi-free standing monolayer graphene on 3C-SiC(111). *Appl. Phys. Lett.* **2011**, *99*, 081904.

[54] Emtsev, K. V.; Speck, F.; Seyller, T.; Ley, L.; Riley, J. D. Interaction, growth, and ordering of epitaxial graphene on SiC{0001} surfaces: A comparative photoelectron spectroscopy study. *Phys. Rev. B* **2008**, *77*, 155303.

[55] Penuelas, J.; Ouerghi, A.; Lucot, D.; David, C.; Gierak, J.; Estrade-Szwarckopf, H.; Andreazza-Vignolle, C. Surface morphology and characterization of thin graphene films on

SiC vicinal substrate. *Phys. Rev. B* **2009**, *79*, 033408.

[56] Jabakhanji, B.; Michon, A.; Consejo, C.; Desrat, W.; Portail, M.; Tiberj, A.; Paillet, M.; Zahab, A.; Cheynis, F.; Lafont, F. et al. Tuning the transport properties of graphene films grown by CVD on SiC(0001): Effect of *in situ* hydrogenation and annealing. *Phys. Rev. B* **2014**, *89*, 085422.

[57] Ostler, M.; Deretzis, I.; Mammadov, S.; Giannazzo, F.; Nicotra, G.; Spinella, C.; Seyller, T.; La Magna, A. Direct growth of quasi-free-standing epitaxial graphene on nonpolar SiC surfaces. *Phys. Rev. B* **2013**, *88*, 085408.

[58] Jayasekera, T.; Xu, S.; Kim, K. W.; Nardelli, M. B. Electronic properties of the graphene/6H-SiC(000-1) interface: A first-principles study. *Phys. Rev. B* **2011**, *84*, 035442.

[59] Ohta, T.; Bostwick, A.; Mcchesney, J. L.; Seyller, T.; Horn, K.; Rotenberg, E. Interlayer interaction and electronic screening in multilayer graphene investigated with angle-resolved photoemission spectroscopy. *Phys. Rev. Lett.* **2007**, *98*, 206802.